



An original interpretation of the wet edge of the surface temperature–albedo space to estimate crop evapotranspiration (SEB-1S), and its validation over an irrigated area in northwestern Mexico

O. Merlin

Centre d'Etudes Spatiales de la Biosphère (CESBIO), UMR5126, 18 avenue Edouard Belin, 31401 Toulouse Cedex 9, France

Correspondence to: O. Merlin (olivier.merlin@cesbio.cnes.fr)

Received: 29 March 2013 – Published in Hydrol. Earth Syst. Sci. Discuss.: 21 May 2013

Revised: 13 August 2013 – Accepted: 19 August 2013 – Published: 30 September 2013

Abstract. The space defined by the pair surface temperature (T) and surface albedo (α), and the space defined by the pair T and fractional green vegetation cover (f_{vg}) have been extensively used to estimate evaporative fraction (EF) from solar/thermal remote sensing data. In both space-based approaches, evapotranspiration (ET) is estimated as remotely sensed EF times the available energy. For a given data point in the $T - \alpha$ space or in the $T - f_{vg}$ space, EF is derived as the ratio of the distance separating the point from the line identified as the dry edge to the distance separating the dry edge and the line identified as the wet edge. The dry and wet edges are classically defined as the upper and lower limit of the spaces, respectively. When investigating side by side the $T - \alpha$ and the $T - f_{vg}$ spaces, one observes that the range covered by T values on the (classically determined) wet edge is different for both spaces. In addition, when extending the wet and dry lines of the $T - \alpha$ space, both lines cross at $\alpha \approx 0.4$ although the wet and dry edges of the $T - f_{vg}$ space never cross for $0 \leq f_{vg} < 1$. In this paper, a new ET (EF) model (SEB-1S) is derived by revisiting the classical physical interpretation of the $T - \alpha$ space to make its wet edge consistent with that of the $T - f_{vg}$ space. SEB-1S is tested over a 16 km by 10 km irrigated area in northwestern Mexico during the 2007–2008 agricultural season. The classical $T - \alpha$ space-based model is implemented as benchmark to evaluate the performance of SEB-1S. Input data are composed of ASTER (Advanced Spaceborne Thermal Emission and Reflection radiometer) thermal infrared, Formosat-2 shortwave, and station-based meteorological data. The fluxes simulated by SEB-1S and the classical $T - \alpha$ space-based model are

compared on seven ASTER overpass dates with the in situ measurements collected at six locations within the study domain. The ET simulated by SEB-1S is significantly more accurate and robust than that predicted by the classical $T - \alpha$ space-based model. The correlation coefficient and slope of the linear regression between simulated and observed ET is improved from 0.82 to 0.93, and from 0.63 to 0.90, respectively. Moreover, constraining the wet edge using air temperature data improves the slope of the linear regression between simulated and observed ET.

1 Introduction

Evapotranspiration (ET) is the boundary condition for the land surface and the atmosphere. An accurate representation of ET is hence required in agronomy, hydrology, meteorology and climatology. For such wide range of applications, ET should be monitored over extensive areas at multiple scales. Whereas ET can be measured at the local (several ha) scale using in situ techniques such as eddy covariance and scintillometry systems, remote sensing technology is recognized as the only viable means to monitor ET spatial variabilities at the irrigation district, catchment, and meso-scales in a temporally and globally consistent and economically feasible manner.

Different methods have been developed to derive ET from remote sensing data including visible, near infrared and thermal infrared bands (Diak et al., 2004; Gowda et al., 2008; Kalma et al., 2008; Verstraeten et al., 2008; Li et al.,

2009; Kustas and Anderson, 2009). They range from semi-empirical ET expressions derived from remotely sensed surface temperature (T) and fractional green vegetation cover (f_{vg}) (e.g., Price, 1990; Moran et al., 1994; Tang et al., 2010; Long and Singh, 2012; Yang and Shang, 2013) or from T and remotely sensed surface albedo (α) (e.g., Menenti et al., 1989; Roerink et al., 2000), to methods estimating ET as the residual term of aerodynamic resistance energy balance equations forced by T , f_{vg} and α (e.g., Norman et al., 1995; Bastiaanssen et al., 1998; Anderson et al., 2007; Cammalleri et al., 2012), and to data assimilation procedures of T into coupled energy and water balance models (e.g., Caparrini et al., 2004; Olioso et al., 2005; Pipunic et al., 2008).

The current thermal-based ET estimation methods greatly vary in complexity. The main advantages of data assimilation methods into physically based SVAT (Soil Vegetation Atmosphere Transfer) models are (1) to integrate many ET-related physical processes such as soil water diffusion and vegetation water uptake in the root zone, and (2) to take into account the uncertainty in both observations and model predictions in an optimal way. Nevertheless, the majority of SVAT models developed since the 1980s (e.g., Noilhan and Planton, 1989) have a large number of parameters that cannot be directly measured at the model application scales (e.g., Franks et al., 1997). Implementation of such complex models is therefore difficult in an operational context. In addition, the over-parameterization issue of SVAT models is further emphasized by the possible need for empirical parameters to fit model predictions with observations (e.g., Bittelli et al., 2008). Last, simple models may perform similarly as more complex models in terms of ET predictions, given they are correctly calibrated (Jiang and Islam, 2003; Margulis et al., 2005; Timmermans et al., 2007). The above mentioned limitations in the application of SVAT models (complexity in operational implementation, over-parameterization and accuracy in ET estimates) are rationales for developing parsimonious ET-oriented modeling approaches which are self-calibrated, i.e., forced by available remotely sensed variables including T , f_{vg} and α .

The $T - f_{vg}$ space, also known as the triangle or trapezoid method, has been extensively used to monitor ET from remote sensing data (Price, 1990; Gillies et al., 1997; Jiang and Islam, 2003; Venturini et al., 2004; Stisen et al., 2008). ET is estimated either from the remotely sensed evaporative fraction (EF) defined as the ratio of ET to the available energy (Jiang and Islam, 1999) or from the remotely sensed evaporative efficiency (EE) defined as the ratio of ET to potential ET (Moran et al., 1994). For a given data point (f_{vg} , T) in the $T - f_{vg}$ space, EF or EE is derived as the ratio of the distance separating the point from the line identified as the dry edge to the distance separating the dry edge and the line identified as the wet edge. The dry and wet edges are classically defined as the upper and lower limit of the spaces, respectively. Since Price (1990), a number of studies have used the $T - f_{vg}$ space for characterizing various ET-

related quantities or phenomena such as surface resistance to ET (e.g., Nemani and Running, 1989), soil moisture (Sandholt et al., 2002; Merlin et al., 2008; Mallick et al., 2009; Kim and Hogue, 2012; Merlin et al., 2013b), land-surface precipitation feedback regimes (Brunsell, 2006), drought (e.g., Wan et al., 2004), fuel moisture content for fire danger management (Chuvieco et al., 2004), and land cover changes (e.g., Julien and Sobrino, 2009).

Alternatively to the $T - f_{vg}$ space, the $T - \alpha$ space has also been proposed to monitor ET over extended areas (Menenti et al., 1989; Roerink et al., 2000). The Simplified Surface Energy Balance Index (S-SEBI, Roerink et al., 2000) determines the wet and dry lines by interpreting the observed correlations between T and α (Menenti et al., 1989). The wet line is defined as the lower limit of the $T - \alpha$ space. It generally has a positive slope as a result of an evaporation control on T . The dry line is defined as the upper limit of the $T - \alpha$ space. It generally has a negative slope as a result of a radiation control on T (Roerink et al., 2000). Similarly to the $T - f_{vg}$ space, EF is derived as the ratio of the distance separating the point (α , T) from the dry line to the distance separating the dry and wet lines, and ET is estimated as a fraction (EF) of available energy. S-SEBI (hereafter named classical $T - \alpha$ space-based model) has been successfully applied in a number of studies (e.g., Gómez et al., 2005; Sobrino et al., 2005, 2007; Fan et al., 2007; Galleguillos et al., 2011b, a).

Both $T - f_{vg}$ and $T - \alpha$ spaces can be used to estimate ET based on a similar identification of dry and wet edges. Since f_{vg} and α provide complementary information on the surface, one would expect synergies between both space-based approaches. For instance, α is sensitive to the total vegetation cover including green (f_{vg}) and senescent vegetation (Merlin et al., 2010, 2012a, b). Consequently the $T - f_{vg}$ space-based approach confuses bare soils and soils fully or partially covered by senescent vegetation, while the $T - \alpha$ space-based approach does not. However, few studies have synergistically combined the $T - f_{vg}$ and $T - \alpha$ spaces. Merlin et al. (2010) and Merlin et al. (2012a) have developed disaggregation methods of T based on observed relationships between T and f_{vg} and observed relationships between T and α -derived fractional senescent vegetation cover. Merlin et al. (2008) developed a disaggregation method (DISPATCH) of surface soil moisture data based on the triangle method. In Merlin et al. (2012b), DISPATCH was improved by representing the water status of vegetation. This involved estimating the water-stressed (maximum) vegetation temperature, which was constrained by one vertex of the four-sided polygon obtained in the $T - \alpha$ space. Nevertheless, the potential synergy between $T - \alpha$ and $T - f_{vg}$ spaces in terms of ET estimation has not been addressed yet.

Another example illustrating the potential synergy between $T - f_{vg}$ and $T - \alpha$ spaces is the determination of temperature endmembers. One major drawback common to $T - f_{vg}$ and $T - \alpha$ space-based approaches is that they both rely on the presence of extreme T . If minimum and maximum

land cover and moisture conditions are not met at the sensor resolution within the study domain, then the remotely sensed EF (or EE) is expected to be systematically biased by a scale factor error. To try and free from the presence of extreme conditions, original algorithms have been proposed to filter outliers in the $T - f_{vg}$ space (Tang et al., 2010), to estimate the maximum vegetation temperature from the $T - \alpha$ space (Merlin et al., 2010, 2012b), or to estimate extreme temperatures using a formulation of aerodynamic resistance (Moran et al., 1994; McVicar and Jupp, 2002; Long et al., 2012) and meteorological data at the specific time of day when the thermal data are acquired (McVicar and Jupp, 1999).

In this context, the main objective of this paper is to develop a monosource (1S) $T - \alpha$ space-based ET model (SEB-1S) that is fully consistent with the $T - f_{vg}$ space-based approach in terms of the physical interpretation of the edges and vertices of the polygons obtained in both $T - \alpha$ and $T - f_{vg}$ spaces. Secondary objectives are (1) to take advantage of the potential synergy between the $T - \alpha$ and $T - f_{vg}$ spaces in the determination of temperature endmembers and (2) to assess the usefulness of constraining the unstressed (minimum) vegetation temperature with available air temperature data. The modeling approach is tested over a 16 km by 10 km irrigated area in northwestern Mexico using ASTER (Advanced Spaceborne Thermal Emission and Reflection radiometer) and Formosat-2 data collected on seven dates during the 2007–2008 agricultural season. Experimental data are described in Sect. 2. In Sect. 3, SEB-1S is described and the classical $T - \alpha$ space-based model is reminded. In Sect. 4, the surface fluxes simulated by both ET models are compared with in situ measurements at six locations.

2 Data collection and preprocessing

The Yaqui experiment was conducted from December 2007 to May 2008 over an irrigated area (27.25° N, 109.88° W) in the Yaqui Valley (state of Sonora) in northwestern Mexico. The campaign focused on a 4 km by 4 km area including 50 % of wheat, the other 50 % being composed of beans, broccoli, chickpeas, chili pepper, corn, oranges, potatoes, safflower and sorghum. The objective of the experiment was to characterize the spatial variability of surface fluxes from the field (hectometric) to kilometeric scale. More details about the Yaqui experiment can be found in Merlin et al. (2010), Fieuzal et al. (2011) and Chirouze et al. (2013). In this paper, the study area is defined as a 16 km by 10 km area containing the 4 km by 4 km Yaqui experimental area and included in all satellite images. During the 2007–2008 agricultural season, seven cloud-free ASTER images were collected over the Yaqui area on 30 December, 23 February, 10 March, 11 April, 27 April, 6 May and 13 May, and 26 cloud-free Formosat-2 images were obtained from 27 December 2007 to 13 May 2008.

Table 1. Flux stations.

Station	Crop
1	Safflower
2	Chili Pepper
3	Chickpeas
4	Potatoes – Sorghum
5	Wheat
6	Wheat

2.1 Flux stations

Seven micro-meteorological stations equipped with an eddy covariance flux measurement system were installed in different fields. For each of the seven sites, the net radiation was acquired with CNR1 or Q7.1 (REBS) radiometers depending on the stations. The soil heat flux was estimated with HUKSEFLUX HFP-01 plates buried at 0.05 m at the top and bottom of the furrow (when applicable). Those data were acquired at a frequency of 10 s and then averaged and recorded each 30 min. Latent and sensible heat fluxes were measured with KH20 fast response hygrometers (Campbell) and Campbell CSAT3 or RM Young 81000 3-D Sonic anemometers at a frequency of 10 Hz and converted to a 30 min average, respectively. Meteorological data including air temperature, solar radiation, relative humidity and wind speed were monitored throughout the agricultural season at a semi-hourly time step from 27 December 2007 until 17 May 2008. Details about the automated data acquisition and flux data quality can be found in Chirouze et al. (2013). In this paper, the six stations listed in Table 1 with at least four ASTER overpass dates of data including the four energy fluxes are used in the comparison analysis.

2.2 ASTER thermal infrared data

ASTER was launched in 1999 on a sun-synchronous platform (NASA's Terra satellite) with 10:30 ECT (Equator crossing time) and a 16 day revisit cycle. The ASTER thermal sensor provides scenes of approximately 60 km by 60 km. Data are collected on request over specified areas. There are five thermal bands centered at 8.30, 8.65, 9.05, 10.60 and 11.63 μm with a 90 m resolution. ASTER official products were downloaded from the Earth Observing System Data Gateway and extracted over the 16 km by 10 km study area. The 90 m resolution surface skin temperature (T) and channel emissivity retrieved by the “temperature and emissivity separation” algorithm (Gillespie et al., 1998; Schmugge et al., 1998) were used. The absolute registration of temperature/emissivity data was performed using a background 8 m resolution Formosat-2 image (Merlin et al., 2010). The broadband surface emissivity (ϵ) was expressed as a linear combination of ASTER channel emissivities using the coefficients in Ogawa and Schmugge (2004).

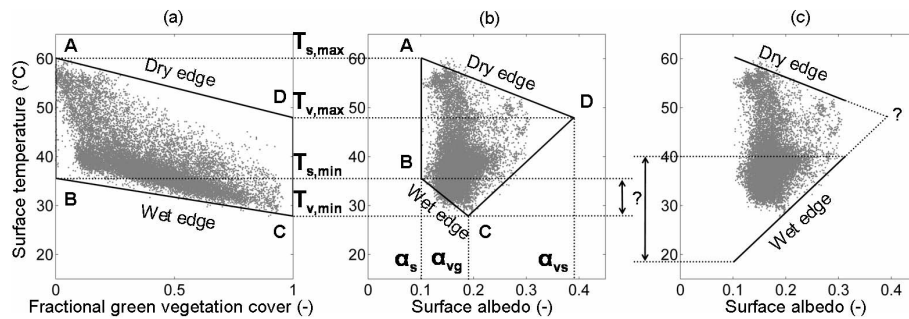


Fig. 1. Consistent interpretation of the edges and vertices of the $T - f_{vg}$ and $T - \alpha$ polygons (a and b), as compared with the classical interpretation of the $T - \alpha$ space (c). Underlying grey points correspond to data on 27 April 2008.

2.3 Formosat-2 red and near-infrared data

Formosat-2 is an Earth observation satellite launched in 2004 by the National Space Organization of Taiwan. It provides high (8 m) resolution images of a particular area every day (09:30 ECT) for four bands (blue, green, red and near-infrared) and with the same view angle (Chern et al., 2008). In this paper, the Formosat-2 data collected on the nearest date from each of the seven ASTER overpass dates were used to estimate f_{vg} and α from the red and near-infrared reflectances aggregated at ASTER thermal sensor resolution. The reason why Formosat-derived instead of ASTER-derived α was used is mainly because the ASTER short-wave infrared (SWIR) data were unusable on four out of the seven ASTER overpass dates (Chirouze et al., 2013): ASTER SWIR detectors are no longer functioning due to anomalously high SWIR detector temperatures (<http://asterweb.jpl.nasa.gov/swir-alert.asp>).

2.3.1 Fractional green vegetation cover

Fractional green (photosynthetically active) vegetation cover is estimated using the expression of Gutman and Ignatov (1998):

$$f_{vg} = \frac{NDVI - NDVI_s}{NDVI_{vg} - NDVI_s}, \quad (1)$$

with $NDVI_{vg}$ corresponding to fully covering green vegetation and $NDVI_s$ to bare soil or to bare soil partially covered by senescent (non-photosynthetically active) vegetation. In the study, $NDVI_{vg}$ and $NDVI_s$ are set to the maximum (0.93) and minimum (0.18) value of the NDVI (Normalized Difference Vegetation Index) observed during the agricultural season within the study domain. NDVI is computed as the ratio of the difference between resampled Formosat-2 near-infrared and red reflectances to their sum. As an illustration, Fig. 1a presents the $T - f_{vg}$ space obtained for data on 27 April 2008.

2.3.2 Surface albedo

Surface albedo is estimated as a weighted sum of resampled Formosat-2 red and near-infrared reflectances with the coefficients given by Weiss et al. (1999) and validated in Bsaibes et al. (2009), and in Chirouze et al. (2013) over the study area. As an illustration, Fig. 1b presents the $T - \alpha$ space obtained for data on 27 April 2008.

3 SEB-1S model

3.1 Surface energy balance

The surface energy balance can be written as

$$R_n - G = H + LE, \quad (2)$$

with R_n (Wm^{-2}) being the surface net radiation, G (Wm^{-2}) the ground heat flux, H (Wm^{-2}) the surface sensible heat flux and LE (Wm^{-2}) the surface latent heat flux. Hence, by setting $EF = LE/(H + LE)$, ET can be derived as

$$LE = EF \times (R_n - G), \quad (3)$$

with $R_n - G$ being the available energy at the surface.

Surface net radiation in Eq. (3) is estimated as

$$R_n = (1 - \alpha) R_g + \epsilon (R_a - \sigma T_a^4), \quad (4)$$

with R_g (Wm^{-2}) being the incoming shortwave radiation, σ ($Wm^{-2}K^{-4}$) the Boltzmann constant, and R_a (Wm^{-2}) the atmospheric longwave radiation computed as

$$R_a = \epsilon_a \sigma T_a^4, \quad (5)$$

with T_a (K) being the air temperature, and ϵ_a (-) the air emissivity estimated as in Brutsaert (1975):

$$\epsilon_a = 1.24 \left(\frac{e_a}{T_a} \right)^{0.143}, \quad (6)$$

with e_a (hPa) being the air vapor pressure.

Ground heat flux in Eq. (3) is estimated as a fraction of Rn:

$$G = \Gamma Rn, \quad (7)$$

and two different Γ expressions are proposed. A first formulation is given by Su (2002):

$$\Gamma = \Gamma_{vg} + (1 - f_{vg}) (\Gamma_s - \Gamma_{vg}), \quad (8)$$

with Γ_{vg} and Γ_s being empirical parameters set to 0.05 (Monteith, 1973) and 0.32 (Kustas and Daughtry, 1989) respectively (Su, 2002). Alternatively, a second Γ formulation is proposed:

$$\Gamma' = \Gamma_{vg} + (1 - EF) (\Gamma_s - \Gamma_{vg}). \quad (9)$$

The physical rationale of Γ' is that G is expected to increase with soil temperature gradient, which is a decreasing function of soil moisture availability. In Eq. (9), soil moisture availability is approximated to EF. Note that Γ and Γ' formulations are equal in the case where $f_{vg} = EF$ (soil evaporation is neglected meaning that the soil surface is dry). Tanguy et al. (2012) have recently proposed a parameterization of G as a function of EF consistent with Eq. (9).

3.2 Model assumptions

EF in Eqs. (3) and (9) is derived from seven endmembers: the maximum soil temperature $T_{s,max}$ corresponding to a dry soil, the minimum soil temperature $T_{s,min}$ corresponding to a water-saturated soil, the temperature of well-watered vegetation $T_{v,min}$, the temperature of water-stressed green or senescent vegetation $T_{v,max}$, the soil albedo α_s , the green vegetation albedo α_{vg} , and the senescent vegetation albedo α_{vs} . Below is a summary of the assumptions made in the following subsections to derive the seven parameters from solar/thermal remote sensing data:

- uniform atmospheric conditions over the study area.
- the four temperature endmembers are uniform at the time of thermal sensor overpass. This notably implies that the aerodynamic resistance to heat transfer is assumed to be uniform by fractional vegetation class.
- the impact of the spatial variability of surface soil moisture and roughness on soil albedo is neglected, meaning that the soil albedo over dry or wet soil surfaces can be approximated to α_s .
- α_s is not larger than α_{vg} . As described in the following subsections, the assumption $\alpha_s \leq \alpha_{vg}$ is essential for drawing the polygon in the $T - \alpha$ space. This assumption generally applies to brown agricultural soils, especially to the Yaqui area where the top 0–20 cm soil was classified as clay. Further developments of SEB-1S will integrate the effects of bright soils (e.g., sands) in the modeling approach.

- α_{vg} is approximately the same for different crops and constant during the agricultural season.
- α_{vs} is approximately the same for different crops and constant during the agricultural season.
- component temperatures are linearly related to component fractions (Merlin and Chehbouni, 2004; Anderson et al., 2007; Long and Singh, 2012).

3.3 Estimating albedo endmembers

α_s is estimated as the minimum α at the time of satellite overpass. α_{vg} is estimated as the temporal mean (over different dates) of the α corresponding to the minimum T within the observation scene ($\alpha_{vg} = 0.19$). α_{vs} is estimated as the maximum α within the observation scene and for the entire agricultural season ($\alpha_{vs} = 0.39$). Figure 1b plots T as a function of α and illustrates the location of α_s , α_{vg} , and α_{vs} for T and α data on 27 April 2008.

3.4 Estimating temperature endmembers

The four temperature endmembers composed of $T_{s,max}$, $T_{s,min}$, $T_{v,min}$, and $T_{v,max}$ are estimated from a synergistic use of both $T - \alpha$ and $T - f_{vg}$ spaces (Merlin et al., 2010, 2012a, b). In particular, a correspondence is built between the four vertices of the $T - \alpha$ and $T - f_{vg}$ polygons as illustrated in Fig. 1a and b and explained below. The $T - f_{vg}$ polygon is defined by the f_{vg} endmembers (0 and 1) and the four temperature endmembers, while the $T - \alpha$ polygon is defined by the three α endmembers (α_s , α_{vg} , α_{vs}), and the same four temperature endmembers as in the $T - f_{vg}$ polygon.

The four edges of the $T - f_{vg}$ polygon (see Fig. 1a) are interpreted as “mixed soil and senescent vegetation” between A and B , “wet surface” between B and C , “full-cover green vegetation” between C and D , and “dry surface” between D and A . The four edges of the $T - \alpha$ polygon (see Fig. 1b) are interpreted as “bare soil” between A and B , “wet surface” between B and C , “full-cover vegetation” between C and D , and “dry surface” between D and A . Note that the segments (AB) and (CD) are interpreted differently in the $T - f_{vg}$ and $T - \alpha$ polygons because f_{vg} (via the NDVI) is a signature of green vegetation cover only while α is a signature of total (green plus senescent) vegetation cover.

Each polygon can provide an estimate of the four temperature endmembers. In the $T - f_{vg}$ polygon, $T_{s,max}$ can be set to the maximum T , $T_{s,min}$ to the minimum T at minimum f_{vg} , $T_{v,min}$ to the minimum T , and $T_{v,max}$ to the maximum T at maximum f_{vg} . Similarly in the $T - \alpha$ polygon, $T_{s,max}$ can be set to the maximum T , $T_{s,min}$ to the minimum T at minimum α , $T_{v,min}$ to the minimum T , and $T_{v,max}$ to the T at maximum α . However, a different approach is preferred herein to improve the robustness, especially in the environments where all surface conditions (dry, wet, bare, full-cover) are not necessarily met. In this paper, the procedure for automatically

estimating temperature endmembers is based on the consistency between both $T - \alpha$ and $T - f_{vg}$ polygons:

- in the $T - \alpha$ polygon, estimates of the minimum soil temperature ($T_{s,min,1}$ at $\alpha = \alpha_s$) and minimum vegetation temperature ($T_{v,min,1}$ at $\alpha = \alpha_{vg}$) are obtained by drawing a line passing through the two points belonging to the wet surface edge, and estimates of maximum soil temperature ($T_{s,max,1}$ at $\alpha = \alpha_s$) and maximum vegetation temperature ($T_{v,max,1}$ at $\alpha = \alpha_{vs}$) are obtained by drawing a line passing through the two points belonging to the dry surface edge. The wet surface edge is defined as the line passing through the point (α_{vg} , T_{min}), with T_{min} being the minimum T , and the point with $\alpha < \alpha_{vg}$ and $f_{vg} < f_{vg,TSMIN}$ such as the slope of the line is maximum (meaning that all the other data points are located above the wet surface edge). $f_{vg,TSMIN}$ is a threshold value (set to 0.5 by default) that stabilizes the determination of the slope. The use of $f_{vg,TSMIN}$ is needed to avoid defining a line (the wet edge in this case) from two data points very close together (Merlin et al., 2012b). Similarly, the dry surface edge is defined as the line passing through the point (α_s , T_{max}), with T_{max} being the maximum T , and the point with $\alpha > \alpha_{vg}$ such as the slope of the line is maximum (meaning that all the other data points are located below the dry surface edge).
- in the $T - f_{vg}$ polygon, alternative estimates of the minimum soil temperature ($T_{s,min,2}$ at $f_{vg} = 0$) and minimum vegetation temperature ($T_{v,min,2}$ at $f_{vg} = 1$) are obtained by drawing a line passing through the two points belonging to the wet surface edge, and alternative estimates of maximum soil temperature ($T_{s,max,2}$ at $f_{vg} = 0$) and maximum vegetation temperature ($T_{v,max,2}$ at $f_{vg} = 1$) are obtained by drawing a line passing through the two points belonging to the dry surface edge. The wet surface edge is defined as the line passing through the point (1, T_{min}) and the point with $f_{vg} < f_{vg,TSMIN}$ such as the slope of the line is maximum (meaning that all the other data points are located above the wet surface edge). Similarly, the dry surface edge is defined as the line passing through the point (0, T_{max}) and the point with $f_{vg} > f_{vg,TVMAX}$ such as the slope of the line is maximum (meaning that all the other data points are located below the dry surface edge). Similarly to $f_{vg,TSMIN}$, $f_{vg,TVMAX}$ is a threshold value (set to 0.5 in this study) that stabilizes the determination of the slope (Merlin et al., 2012b).
- an estimate of the four temperature endmembers is obtained by averaging the two temperature endmember sets 1 and 2:

$$T_{s,max} = T_{s,max,1} = T_{s,max,2} = T_{max}, \quad (10)$$

$$T_{s,min} = (T_{s,min,1} + T_{s,min,2})/2, \quad (11)$$

$$T_{v,min} = T_{v,min,1} = T_{v,min,2} = T_{min}, \quad (12)$$

$$T_{v,max} = (T_{v,max,1} + T_{v,max,2})/2. \quad (13)$$

In this study, two different strategies are investigated to further constrain the wet edge ($T_{v,min}$ and $T_{s,min}$) of both polygons. The first strategy is to force $T_{v,min,1} = T_{v,min,2} = T_a$, by assuming that air temperature is a better proxy for $T_{v,min}$ than T_{min} . The rationale for constraining $T_{v,min}$ is to investigate a possibility to improve the robustness of the methodology for estimating temperature endmembers (and hence EF/ET) from available meteorological data, especially over areas where the full-cover, well-watered green vegetation condition is not met at the observation resolution. The second strategy is to adjust $f_{vg,TSMIN}$ so that the absolute difference between $T_{s,min,1}$ and $T_{s,min,2}$ is minimized. The rationale for optimizing $f_{vg,TSMIN}$ is to foster the consistency between both $T - \alpha$ and $T - f_{vg}$ polygons at the wet soil vertex, and to potentially provide a more accurate $T_{s,min}$ value.

3.5 Classical $T - \alpha$ space-based EF model

EF in Eq. (3) can be estimated by the classical $T - \alpha$ space-based approach. In S-SEBI, the wet edge has a positive slope as a result of an evaporation control on T and the dry edge has a negative slope as a result of a radiation control on T (Roerink et al., 2000). Figure 1c represents the wet and dry edges as classically identified in the $T - \alpha$ space for data on 27 April 2008. When investigating side by side Fig. 1b and c, one observes that the classically determined wet and dry edges correspond to (CD) and (AD), respectively.

Figure 2a graphically illustrates how the EF of a given point J in the $T - \alpha$ space is calculated in S-SEBI: EF is derived as the ratio of the distance separating the point $J = (\alpha_J, T_J)$ from the dry edge to the distance separating the dry and wet edges. Analytically:

$$EF = \frac{T_I - T_J}{T_I - T_K}, \quad (14)$$

with T_I being the surface temperature if the pixel surface was fully dry, and T_K the surface temperature if the pixel surface was fully wet. T_I and T_K are estimated at $\alpha_J = \alpha_I = \alpha_K$ on (AD) and (CD), respectively (see Figs. 1b, c and 2a):

$$T_I = T_{s,max} - \frac{\alpha_J - \alpha_s}{\alpha_{vs} - \alpha_s} (T_{s,max} - T_{v,max}) \quad (15)$$

and

$$T_K = T_{v,min} + \frac{\alpha_J - \alpha_{vg}}{\alpha_{vs} - \alpha_{vg}} (T_{v,max} - T_{v,min}). \quad (16)$$

At this point it is worth noting that the classical interpretation of the wet edge in the $T - \alpha$ space (see Fig. 1c) is not consistent with that in the $T - f_{vg}$ space (see Fig. 1a). In fact, two different inconsistencies clearly appear in Fig. 1.

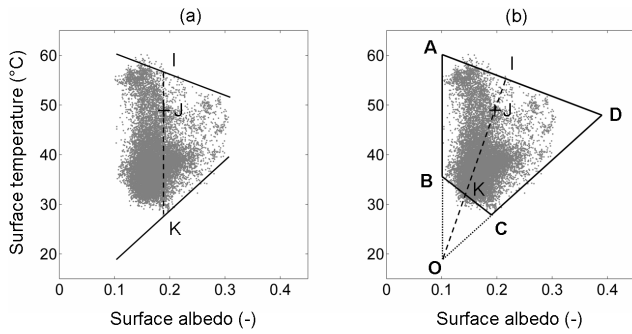


Fig. 2. EF is computed as IJ/IK in S-SEBI (a) and SEB-1S (b). Underlying grey points correspond to data on 27 April 2008.

First, the range covered by T values on the (classically determined) wet edge is different for both spaces (see Fig. 1a and c). Second, when extending the classically determined wet and dry lines of the $T - \alpha$ space (see Fig. 1c), both lines cross at $\alpha \approx 0.4$ although the wet and dry edges of the $T - f_{vg}$ space never cross for $0 \leq f_{vg} < 1$. The crossing of the wet and dry edges for a physical value of α is not acceptable since a surface cannot be at the same time fully dry, and transpiring at potential rate. The two above mentioned inconsistencies in the classical interpretation of the $T - \alpha$ space, and the potential synergy between $T - \alpha$ and $T - f_{vg}$ polygons, both provide the opportunity to propose an original interpretation of the $T - \alpha$ space as explained below.

3.6 SEB-1S EF model

In SEB-1S, the wet edge of the $T - \alpha$ space is defined as (BC) instead of (CD) (see Fig. 1). SEB-1S is thus consistent with the classical interpretation of the $T - f_{vg}$ space (see Fig. 1a and b). Figure 2b graphically illustrates how the EF of a given point J in the $T - \alpha$ space is calculated in SEB-1S: EF is derived as the ratio of the distance separating the point $J = (\alpha_J, T_J)$ from the dry edge to the distance separating the dry and wet edges. EF is computed as in Eq. (14) except that T_I and T_K are now estimated from the wet edge (BC) . In practice, the three-step procedure is described below (see Fig. 2b for graphical visualization).

- The bare soil line (AB) and the full-cover line (CD) cross each other at $O = (\alpha_O, T_O)$:

$$\alpha_O = \alpha_s, \tag{17}$$

$$T_O = T_{v,\min} - \frac{\alpha_{vg} - \alpha_s}{\alpha_{vs} - \alpha_{vg}} (T_{v,\max} - T_{v,\min}). \tag{18}$$

- The line (OJ) crosses the wet edge at $K = (\alpha_K, T_K)$:

$$\alpha_K = \alpha_s + \frac{T_{s,\min} - T_O}{a_{OJ} - a_{BC}}, \tag{19}$$

$$T_K = T_{s,\min} + a_{BC} (\alpha_K - \alpha_s), \tag{20}$$

and the dry edge at $I = (\alpha_I, T_I)$:

$$\alpha_I = \alpha_s + \frac{T_{s,\max} - T_O}{a_{OJ} - a_{AD}}, \tag{21}$$

$$T_I = T_{s,\max} + a_{AD} (\alpha_I - \alpha_s), \tag{22}$$

with a_{OJ} , a_{BC} and a_{AD} the slope of (OJ) , (BC) and (AD) respectively:

$$a_{OJ} = \frac{T_J - T_O}{\alpha_J - \alpha_s}, \tag{23}$$

$$a_{BC} = \frac{T_{v,\min} - T_{s,\min}}{\alpha_{vg} - \alpha_s}. \tag{24}$$

$$a_{AD} = \frac{T_{v,\max} - T_{s,\max}}{\alpha_{vs} - \alpha_s}. \tag{25}$$

- Given the temperature endmembers, albedo endmembers, and the pair (α_J, T_J) , one is able to compute $EF = IJ/IK$ as

$$EF = \text{sgn}(\alpha_I - \alpha_J) \times \frac{[(\alpha_J - \alpha_I)^2 + (T_J - T_I)^2]^{0.5}}{[(\alpha_K - \alpha_I)^2 + (T_K - T_I)^2]^{0.5}}. \tag{26}$$

with $\text{sgn}(x)$ being the sign function returning $x/|x|$.

Note that point O in Fig. 2b is defined as the homothetic center of (AD) and (BC) so that for any point J in the polygon $ABCD$, I belongs to (AD) and K belongs to (BC) .

4 Application

The simulation results of SEB-1S and the classical $T - \alpha$ space-based EF model are compared on the seven ASTER overpass dates with the in situ measurements collected by six flux stations. Comparisons are made at the pixel scale by extracting the ASTER pixels including a flux station.

4.1 Temperature endmembers

Figure 3a plots T_{\min} as a function of T_a for all ASTER overpass dates. On 11 April 2008, a significant difference of about 5°C is obtained between T_{\min} and T_a . This difference may be due to the presence of standing water in some irrigated fields or advection effects caused by strong differences in T between the various fields. Note that 11 April 2008 corresponds to the date with the largest available energy among the seven ASTER overpass dates. When removing this particular date from the comparison, the root mean square difference, correlation coefficient, and slope of the linear regression between T_{\min} and T_a is 1.8°C , 0.91, and 1.0, respectively. As a summary, setting $T_{v,\min,1} = T_{v,\min,2} = T_{\min}$ appears to be mostly valid over the Yaqui irrigated area, and setting $T_{v,\min,1} = T_{v,\min,2} = T_a$ provides a significantly different $T_{v,\min}$ estimate around the seasonal peak of ET.

The strategy for improving the estimation of $T_{s,\min}$ is investigated by plotting $T_{s,\min,2}$ as a function of $T_{s,\min,1}$

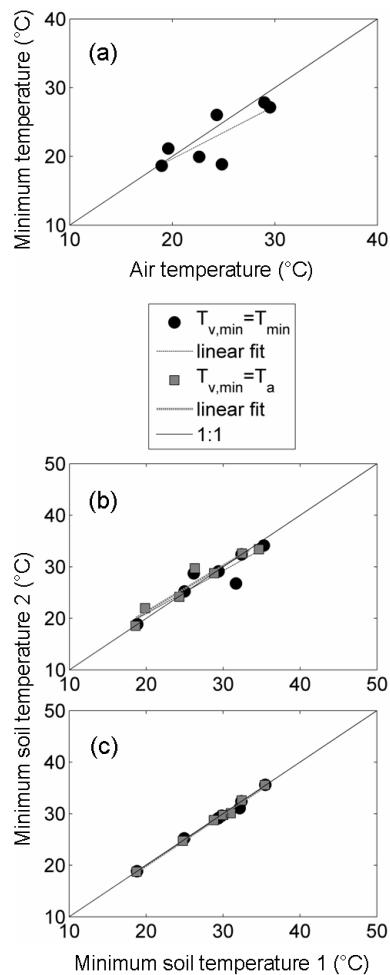


Fig. 3. T_{\min} is plotted versus T_a (a), and $T_{s,\min,1}$ and $T_{s,\min,2}$ are intercompared for both $T_{v,\min} = T_{\min}$ and $T_{v,\min} = T_a$ cases, and for $f_{vg,TSMIN} = 0.5$ (b) and daily optimized $f_{vg,TSMIN}$ (c) separately.

for $f_{vg,TSMIN} = 0.5$ and daily optimized $f_{vg,TSMIN}$ cases in Fig. 3b and c, respectively. In both cases, the minimum soil temperatures retrieved from the $T_{v,\min} = T_{\min}$ and $T_{v,\min} = T_a$ assumptions are intercompared. It is visible that setting $T_{v,\min} = T_a$ generally has a little effect on $T_{s,\min}$ in both $f_{vg,TSMIN} = 0.5$ and daily optimized $f_{vg,TSMIN}$ cases. However, adjusting $f_{vg,TSMIN}$ allows to significantly reduce the absolute difference between $T_{s,\min,1}$ and $T_{s,\min,2}$, and to stabilize the retrieval of $T_{s,\min}$ from both $T - \alpha$ and $T - f_{vg}$ polygons. In the following, $T_{s,\min}$ is consequently derived from the daily optimized $f_{vg,TSMIN}$, for both $T_{v,\min} = T_{\min}$ and $T_{v,\min} = T_a$ assumptions.

Figure 4 plots side by side the $T - \alpha$ and $T - f_{vg}$ spaces for each of the seven ASTER overpass dates. Each space is overlaid with the polygon built from the $T_{v,\min} = T_{\min}$ assumption, and with the polygon built from the $T_{v,\min} = T_a$ assumption. As in Merlin et al. (2013a), one observes that both the $T - \alpha$ and $T - f_{vg}$ spaces significantly vary from date to date. This

change is notably explained by the presence of bright senescent vegetation towards the end of the agricultural season. Despite the strong temporal variability of $T - \alpha$ spaces however, the automatically retrieved $T - \alpha$ polygons are relatively stable across the agricultural season, meaning that the four edges are robustly determined regardless of crop phenological stages. It is suggested that both polygons work in synergy to estimate temperature endmembers. When comparing the polygons obtained from the two strategies ($T_{v,\min} = T_{\min}$ and $T_{v,\min} = T_a$), one observes that both polygons are generally consistent on all dates, although some significant differences are visible especially for the full-cover, unstressed green vegetation vertex.

Figure 5 plots the time series of f_{vg} , α and T for data extracted over each flux station separately. The time series of f_{vg} indicates various crop phenological stages at all ASTER observations dates, meaning that minimum and maximum vegetation covers are generally met within the study domain, consistent with the $T - f_{vg}$ spaces on all dates (see Fig. 4). When looking at the curve for the dominant crop type (wheat), the seasonal cycle –including growing and senescence– is very well marked. The time series of α provides information consistent with the $T - \alpha$ spaces plotted in Fig. 4: α is close to 0.18 for f_{vg} larger than 0.5, α is generally lower than 0.18 for f_{vg} lower than 0.5, and α is generally larger than 0.18 during the senescence. For the wheat crop, the increase in α during the senescence is very significant with values reaching 0.32 on 13 May. The time series of T is more complex to interpret since it is a function of both the surface state and the atmospheric conditions at ASTER overpass time. However, it is still visible that T generally decreases with f_{vg} , consistent with the $T - f_{vg}$ spaces plotted in Fig. 4.

4.2 Available energy

Figure 6 plots the simulated versus observed net radiation and ground heat fluxes at the six flux stations. Since wheat is the dominant cropping type within the area, results for station 5 and 6 are highlighted with black markers. Statistics are reported in Table 2 in terms of correlation coefficient, root mean square difference, mean difference and slope of the linear regression between simulated and observed data. The uncertainty in modeled net radiation and ground heat flux over the Yaqui area, with a root mean square error of about $40\text{--}50 \text{ W m}^{-2}$ for both fluxes, is comparable with other studies (Chirouze et al., 2013). When comparing the ground heat flux (G) simulated using the Γ formulation (Fig. 6b) with that (G') simulated using the Γ' formulation (Fig. 6c), one observes that the scatter is significantly reduced for the latter. Consequently, it seems that EF can be appropriately used instead of f_{vg} to parameterize G as a fraction of Rn. Chirouze et al. (2013) indicated that the sensors at station 3 (chickpeas) significantly overestimated ground heat flux. When removing this station from the comparison, the root mean square

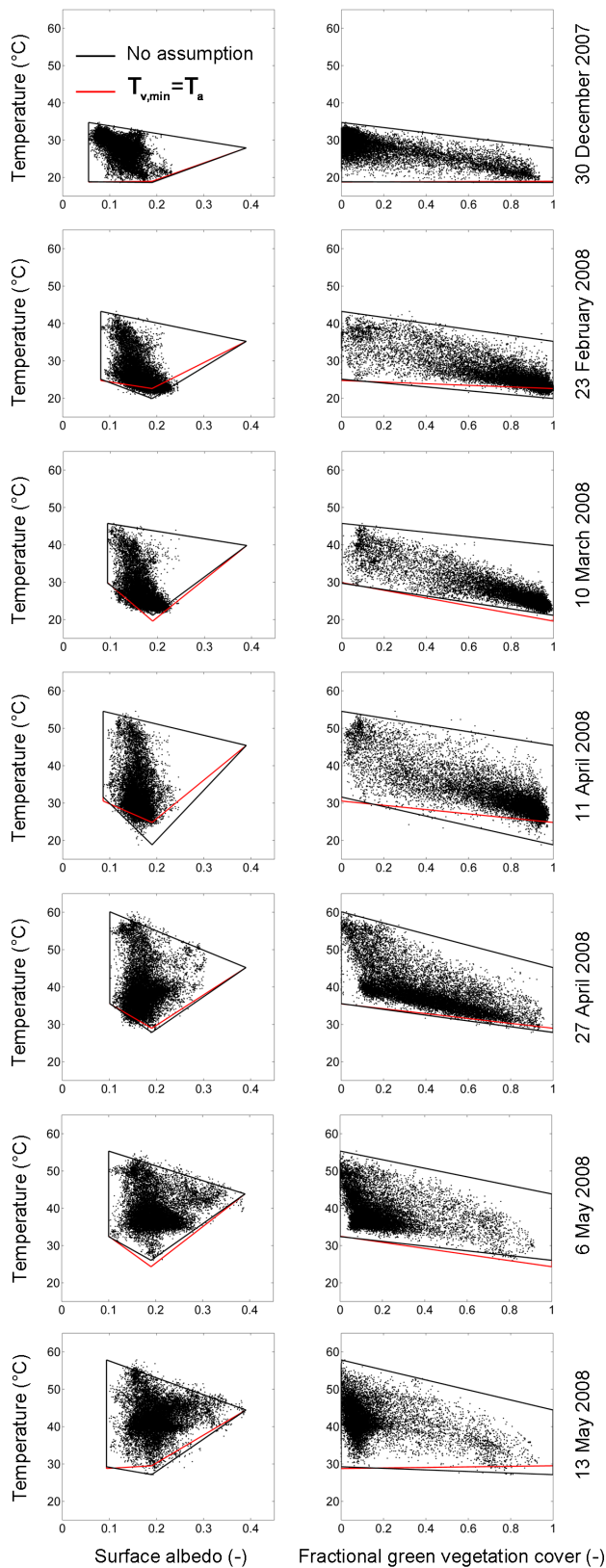


Fig. 4. For each ASTER overpass date, the $T - \alpha$ and $T - f_{vg}$ spaces are overlaid with the polygon built from $T_{v,min} = T_{min}$ (black) and the polygon built from $T_{v,min} = T_a$ (red).

Table 2. Correlation coefficient (R), root mean square difference (RMSD), mean bias and slope of the linear regression between simulated and observed fluxes.

Flux	$T_{v,min}$	R	RMSD	Bias	Slope
Rn	NA	0.88	40	-3	0.87
G	NA	0.51	54	2	0.40
G'	T_{min}	0.68	46	-12	0.38
G'	T_a	0.66	47	-15	0.40

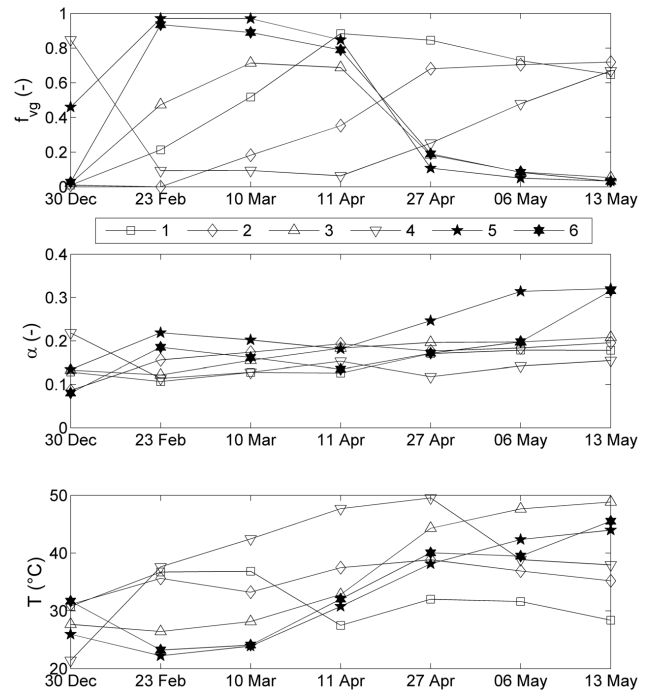


Fig. 5. Time series (arbitrary timescale) of f_{vg} , α and T at each flux station separately.

difference, mean difference, correlation coefficient and slope of the linear regression between simulated and observed ground heat flux is 30 Wm^{-2} , 1 Wm^{-2} , 0.67, and 0.54, respectively. When comparing the ground heat flux (G') simulated using the EF derived from the $T_{v,min} = T_{min}$ assumption (Fig. 6c) with that simulated using the EF derived from the $T_{v,min} = T_a$ assumption (Fig. 6d), no major difference is obtained between the two.

4.3 ET

The classical $T - \alpha$ space-based approach and SEB-1S both estimate ET as EF times the available energy ($Rn - G$). To quantify the impact of the modeling of available energy on ET predictions, Fig. 7a-d present the ET simulated using the observed available energy and Fig. 8a-d present the ET simulated using the modeled available energy. In each case, both (classical $T - \alpha$ space-based and SEB-1S) EF models

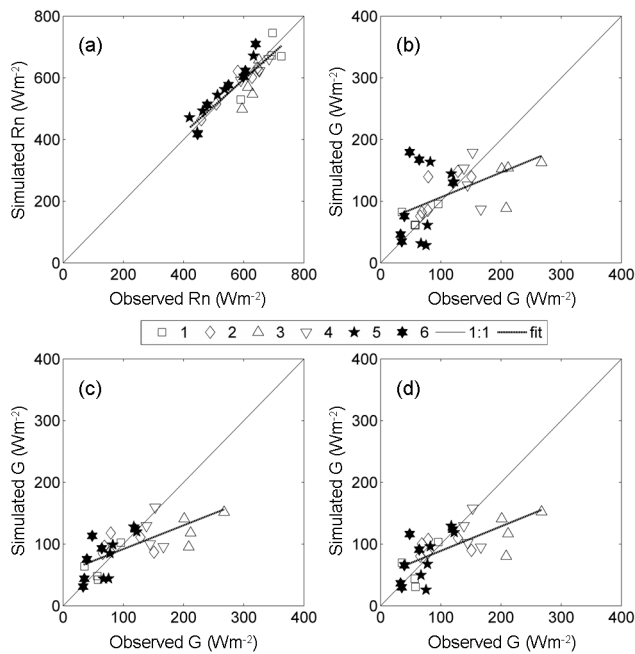


Fig. 6. Modeled net radiation (a), ground heat flux using Γ formulation (b), ground heat flux using Γ' formulation and $T_{v,\min} = T_{\min}$ assumption (c), and ground heat flux using Γ' formulation and $T_{v,\min} = T_a$ assumption (d) versus station measurements.

Table 3. Correlation coefficient, root mean square difference, mean bias and slope of the linear regression between simulated and observed ET.

EF model	$T_{v,\min}$	Rn – G	R	RMSD	Bias	Slope
$T - \alpha$	T_{\min}	Station	0.82	100	-17	0.64
SEB-1S	T_{\min}	Station	0.93	65	11	0.90
$T - \alpha$	T_a	Station	0.84	93	-3	0.69
SEB-1S	T_a	Station	0.93	67	20	0.93
$T - \alpha$	T_{\min}	SEB-1S (G')	0.82	99	-17	0.66
SEB-1S	T_{\min}	SEB-1S (G')	0.91	74	19	0.91
$T - \alpha$	T_a	SEB-1S (G')	0.83	96	-2	0.71
SEB-1S	T_a	SEB-1S (G')	0.90	84	31	0.95

are compared for the $T_{v,\min} = T_{\min}$ and $T_{v,\min} = T_a$ cases, separately. Statistical results are provided in Table 3 in terms of correlation coefficient, root mean square difference, mean difference, and slope of the linear regression between simulated and observed LE. It appears that the modeled available energy slightly degrades or slightly improves ET model predictions, and that the approach for estimating EF has a much stronger impact on ET estimates. In terms of correlation coefficient and slope of the linear regression between simulated and observed LE in particular, modeled available energy is responsible for a 0.00–0.03 and 0.01–0.02 difference, respectively, while modeled EF is responsible for a 0.07–0.11 and 0.24–0.26 difference, respectively.

In the case where the available energy is provided by station measurements, setting $T_{v,\min} = T_a$ improves all the sta-

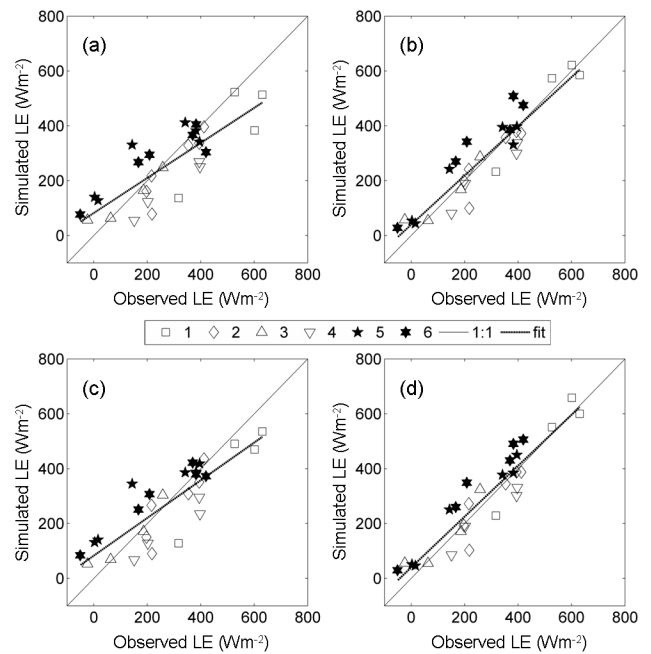


Fig. 7. The ET simulated by the classical $T - \alpha$ space-based approach (a and c) and by SEB-1S (b and d) using observed available energy is plotted versus station measurements. The top and bottom lines correspond to $T_{v,\min} = T_{\min}$ and $T_{v,\min} = T_a$, respectively.

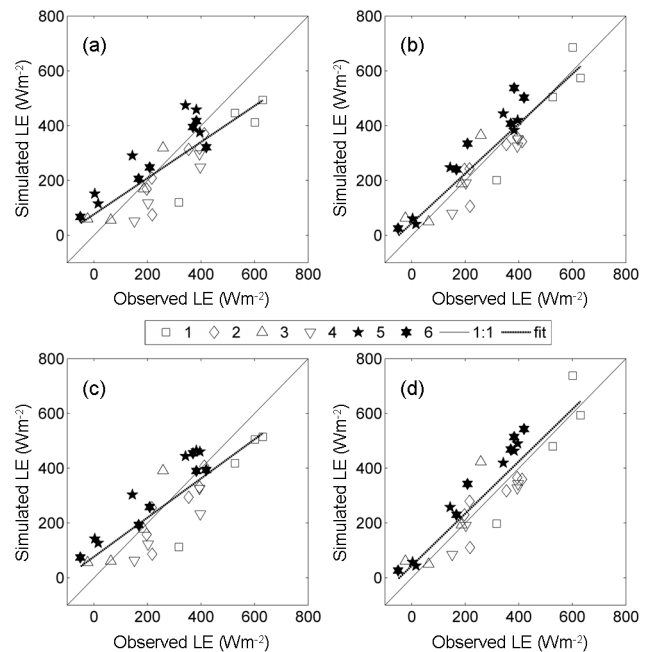


Fig. 8. Same for Fig. 7 but using modeled available energy.

tistical results of the classical $T - \alpha$ space-based model. Regarding SEB-1S, the slope of the linear regression between simulated and observed ET is improved from 0.90 to 0.93 by setting $T_{v,\min} = T_a$, with a constant correlation coefficient estimated as 0.93. In the case where the available energy

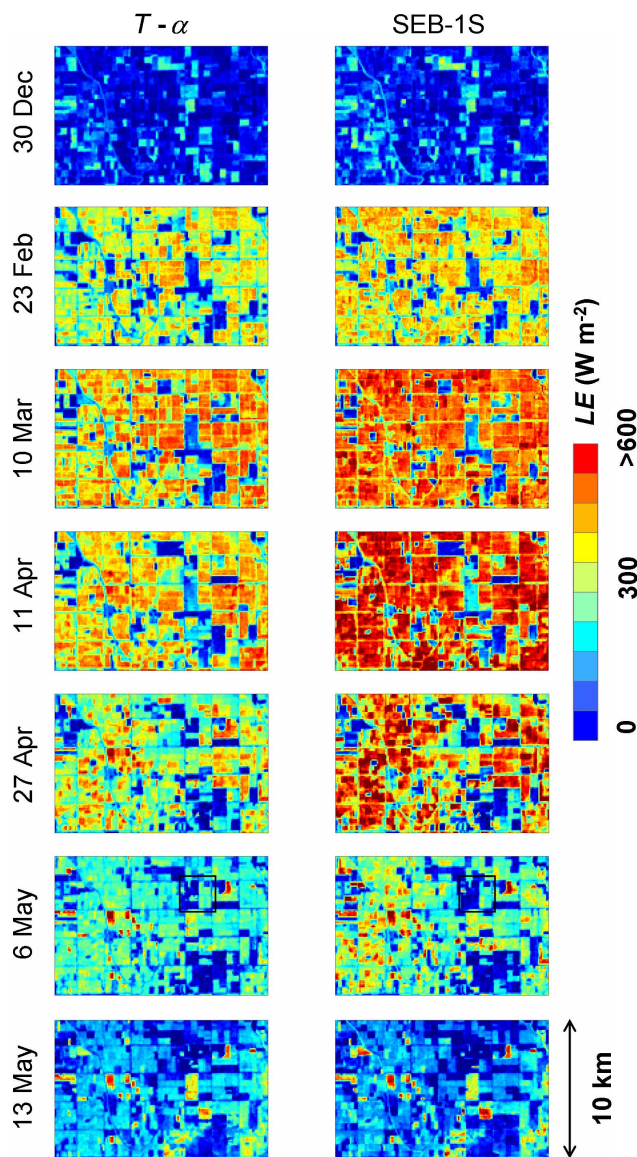


Fig. 9. Images on the seven ASTER overpass dates of the ET simulated by the classical $T - \alpha$ space-based model and SEB-1S. The enclosed sub-area for data on 6 May 2008 is enlarged in Fig. 10.

is modeled, similar improvements are observed by setting $T_{v,\min} = T_a$ instead of $T_{v,\min} = T_{\min}$ for both the classical $T - \alpha$ polygon-based model and SEB-1S. When extracting the data from the two wheat sites, the correlation coefficient and slope of the linear regression between the ET simulated by SEB-1S and observations is improved from 0.95 to 0.97 and from 0.90 to 0.99, respectively (case of observed energy, see Fig. 7b and d). Consequently, forcing the minimum vegetation temperature using available air temperature seems to foster the robustness of both polygon-based models. However, the improvement in ET estimates by setting $T_{v,\min} = T_a$ is relatively small, meaning that estimating $T_{v,\min}$ as T_{\min} is a satisfying option over the irrigated Yaqui area.

Although SEB-1S very significantly improves the correlation coefficient and slope of the linear regression between simulated and observed ET in all configurations, a positive bias is obtained of about 10–20 and 20–30 W m^{-2} for modeled and observed available energy, respectively (see Table 3). The persistent bias is also visible in Figs. 7 and 8, especially for the wheat sites. This may be due to the fact that the current version of SEB-1S neglects the sensible heat flux over fully transpiring (well-watered) pixels, and hence systematically overestimates ET over those areas. One way to overcome this effect, and to probably reduce the positive bias would be to estimate EE instead of EF. Part of the differences obtained between modeled and observed ET may also be due to possible changes in size and shape of the spatial fetch of flux towers, and to the non-closure of the energy balance at eddy covariance sites (Chirouze et al., 2013).

Figure 9 presents the images on the seven ASTER overpass dates of the ET simulated by the classical $T - \alpha$ polygon-based model, and SEB-1S. A visual intercomparison indicates that the main differences between the two models is the larger range of the ET values predicted by SEB-1S. Moreover, the spatial distribution of ET seems to be more heterogeneous during the growing period for the classical $T - \alpha$ space-based polygon, especially on 23 February, 10 March and 11 April. During the senescence of most crops (around 27 April) the spatial heterogeneity is quite pronounced for both models, while SEB-1S still provides larger ET estimates. The spatial distribution and mean level of ET is relatively similar for both ET models at the beginning (30 December) and at the end (6 and 13 May) of the agricultural season. However, significant differences may appear when looking at details. For instance, the ET image on 6 May over a 2 km sub-area of the study domain is enlarged in Fig. 10. The classical $T - \alpha$ space-based model provides ET values of about 300 W m^{-2} in the southwestern corner of the 1 km area, whereas SEB-1S predicts low values (close to 0). This sub-area corresponds to data points located in the right hand side of the $T - \alpha$ space (with α values close to α_{vs}) and close to (CD) (see the $T - \alpha$ polygon illustrated in Fig. 2b). For large α values, the classically determined $EF = IJ/IK$ (see Fig. 2a) is highly uncertain because both distances IJ and IK become very small, and the ratio IJ/IK is undetermined. On the contrary, the EF estimated in SEB-1S (see Fig. 2b) becomes small at large α values, because for data points J close to D , IJ tends to 0, and IK to DC .

5 Conclusions

A new solar/thermal-based ET model (SEB-1S) is developed by providing an original interpretation of the $T - \alpha$ space. The main ideas behind SEB-1S are (1) to make the physical interpretation of the edges and vertices of the polygons in $T - \alpha$ and $T - f_{vg}$ spaces fully consistent (2) to derive EF from the $T - \alpha$ space based on this new interpretation and

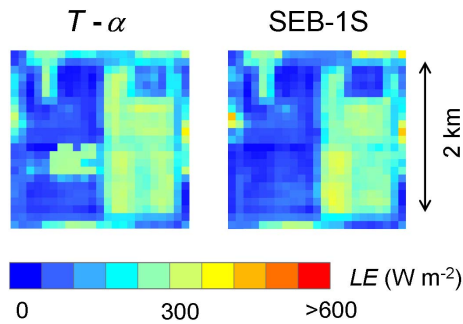


Fig. 10. Images on 6 May 2008 of the ET simulated by the classical $T - \alpha$ space-based model and SEB-1S over a sub-area of the study domain.

(3) to take advantage of the potential synergy between the $T - \alpha$ and $T - f_{vg}$ spaces in the determination of temperature endmembers.

SEB-1S is tested over a 16 km by 10 km irrigated area in northwestern Mexico during the 2007–2008 agricultural season. The classical $T - \alpha$ space-based model is also implemented over the study area, as benchmark to evaluate the performance of SEB-1S. For both models input data are composed of ASTER thermal infrared, resampled Formosat-2 shortwave, and station-based meteorological data. The fluxes simulated by SEB-1S and by the classical $T - \alpha$ space-based model are compared on seven ASTER overpass dates with the in situ measurements collected at six locations within the study domain. It is found that the uncertainties in EF have a much larger impact on ET estimates than the uncertainties in available energy. The EF modeled by SEB-1S improves the correlation coefficient and slope of the linear regression between simulated and observed ET from 0.82 to 0.93, and from 0.63 to 0.90, respectively. Moreover, constraining $T_{v,min}$ using air temperature data improves the slope of the linear regression between simulated and observed ET from 0.90 to 0.93.

Despite the remarkable robustness of SEB-1S on the seven ASTER dates over the Yaqui area, a persistent bias of about 20 W m^{-2} is obtained in simulated ET. This may be due to the fact that the current version of SEB-1S neglects the sensible heat flux over fully transpiring (well-watered) pixels, and hence systematically overestimates ET over those areas. One way to overcome this effect, and to probably reduce the positive bias would be to estimate EE instead of EF. Other issues to be addressed in the short term include:

- confirming the potential of this methodology would require further evaluation in different agricultural sites. Several field experiments are already planned in Chile, France, Morocco and Spain to collect eddy covariance measurements under a range of pedo-hydro-climatic conditions.

- investigating possibilities to further constrain the dry edge ($T_{s,max}$ and $T_{v,max}$). A robust temperature end-member algorithm is needed to extend the validity domain of SEB-1S to less heterogeneous rainfed areas, and to remote sensing data collected at coarser spatial resolution (Long and Singh, 2013).
- assessing the utility of discretizing the surface into several components to improve the accuracy in modeled ET. Merlin et al. (2013a) have recently developed a four-source ET model (SEB-4S) based on a synergistic use of both $T - \alpha$ and $T - f_{vg}$ spaces. SEB-4S represents four components of agricultural fields including bare soil, unstressed green (photosynthetically-active) vegetation, water-stressed green vegetation, and senescent vegetation. Since the above four components have distinct radiative and turbulent exchange properties, comparing SEB-1S and SEB-4S results may help identify the impact of each surface component on modeled ET.
- a revisit cycle of 16 days for ASTER/Landsat (in cloud free conditions) is long compared to rapid changes in relation with rainfall or irrigation for instance, which makes the practical application of ASTER/Landsat data to ET monitoring relatively indirect. Before the advent of thermal infrared missions with shorter revisit cycles (Lagouarde et al., 2013), several techniques could be used to disaggregate low resolution (e.g., MODIS) temperature data at high temporal resolution (e.g., Merlin et al., 2010, 2012a) prior to running SEB-1S at high spatiotemporal resolution.

Acknowledgements. The author is grateful to Gilles Boulet, Ghani Chehbouni, Jonas Chirouze, Benoît Duchemin and Lionel Jarlan for providing the Yaqui data set. Funding from the French space agency (Centre National d’Etudes Spatiales, CNES) for the MiSTIGRI (MicroSatellite for Thermal Infrared Ground surface Imaging) phase A study, as well as the FORMOSAT acquisition, the MISTRALS (Mediterranean Integrated Studies at Regional And Local Scales) SICMed (Continental Surfaces and Interfaces in the Mediterranean area) program, the European FP7 SIRIUS, the PLEIADES (Participatory multi-Level EO-assisted tools for Irrigation water management and Agricultural Decision-Support) program as well as the IRD (Institut de Recherche pour le Développement), the ITSON (Instituto Tecnológico de SONora), the University of Sonora and the Cadi Ayyad University (Morocco) in the setting up of the “Yaqui experiment” are gratefully acknowledged. This study is part of the MIXMOD-E project funded by the French ANR (Agence Nationale de la Recherche).

Edited by: N. Ursino



The publication of this article is financed by CNRS-INSU.

References

- Anderson, M. C., Norman, J. M., Mecikalski, J. R., Otkin, J. A., and Kustas, W. P.: A climatological study of evapotranspiration and moisture stress across the continental United States based on thermal remote sensing: 1. Model formulation, *J. Geophys. Res.*, 112, D10117, doi:10.1029/2006JD007506, 2007.
- Bastiaanssen, W. G. M., Menenti, M., Feddes, R. A., and Holtslag, A. A. M.: A remote sensing surface energy balance algorithm for land (SEBAL) 1. Formulation, *J. Hydrol.*, 212–213, 198–212, 1998.
- Bittelli, M., Ventura, F., Campbell, G. S., Snyder, R. L., Gallegati, F., and Pisa, P. R.: Coupling heat, water vapor, and liquid water fluxes to compute evaporation in bare soils, *J. Hydrol.*, 362, 191–205, doi:10.1016/j.jhydrol.2008.08.014, 2008.
- Brunsell, N. A.: Characterization of land-surface precipitation feedback regimes with remote sensing, *Remote Sens. Environ.*, 100, 200–211, doi:10.1016/j.rse.2005.10.025, 2006.
- Brutsaert, W.: On a derivable formula for long-wave radiation from clear skies, *Water Resour. Res.*, 11, 742–744, 1975.
- Bsaibes, A., Courault, D., Baret, F., Weiss, M., Olioso, A., Jacob, F., Hagolle, O., Marloie, O., Bertrand, N., Desfond, V., and Kzemipour, F.: Albedo and LAI estimates from FORMOSAT-2 data for crop monitoring, *Remote Sens. Environ.*, 113, 716–729, doi:10.1016/j.rse.2008.11.014, 2009.
- Cammalleri, C., Anderson, M. C., Ciraolo, G., D'Urso, G., Kustas, W. P., Loggia, G. L., and Minacapilli, M.: Applications of a remote sensing-based two-source energy balance algorithm for mapping surface fluxes without in situ air temperature observations, *Remote Sens. Environ.*, 124, 502–515, doi:10.1016/j.rse.2012.06.009, 2012.
- Caparrini, F., Castelli, F., and Entekhabi, D.: Estimation of surface turbulent fluxes through assimilation of radiometric surface temperature sequences, *J. Hydrometeorol.*, 5, 145–159, 2004.
- Chern, J.-S., Ling, J., and Weng, S.-L.: Taiwan's second remote sensing satellite, *Acta Astronautica*, 63, 1305–1311, doi:10.1016/j.actaastro.2008.05.022, 2008.
- Chirouze, J., Boulet, G., Jarlan, L., Fieuzal, R., Rodriguez, J. C., Ez-zahar, J., Er-Raki, S., Bigeard, G., Merlin, O., Garatuza-Payan, J., Watts, C., and Chehbouni, G.: Inter-comparison of four remote sensing based surface energy balance methods to retrieve surface evapotranspiration and water stress of irrigated fields in semi-arid climate, *Hydrol. Earth Syst. Sci. Discuss.*, 10, 895–963, doi:10.5194/hessd-10-895-2013, 2013.
- Chuvieco, E., Cocero, D., Riaño, D., Martín, P., Martínez-Vega, J., de la Riva, J., and Pérez, F.: Combining NDVI and surface temperature for the estimation of live fuel moisture content in forest fire danger rating, *Remote Sens. Environ.*, 92, 322–331, doi:10.1016/j.rse.2004.01.019, 2004.
- Diak, G. R., Mecikalski, J. R., Anderson, M. C., Norman, J. M., Kustas, W. P., Torn, R. D., and de Wolf, R. L.: Estimating land surface energy budgets from space, *B. Am. Meteorol. Soc.*, 85, 65–78, doi:10.1175/BAMS-85-1-65, 2004.
- Fan, L., Liu, S., Bernhofer, C., Liu, H., and Berger, F. H.: Regional land surface energy fluxes by satellite remote sensing in the upper Xilin river watershed (inner Mongolia, China), *Theor. Appl. Climatol.*, 88, 231–245, doi:10.1007/s00704-006-0241-9, 2007.
- Fieuzal, R., Duchemin, B., Jarlan, L., Zribi, M., Baup, F., Merlin, O., Hagolle, O., and Garatuza-Payan, J.: Combined use of optical and radar satellite data for the monitoring of irrigation and soil moisture of wheat crops, *Hydrol. Earth Syst. Sci.*, 15, 1117–1129, doi:10.5194/hess-15-1117-2011, 2011.
- Franks, S. W., Beven, K. J., Quinn, P. F., and Wright, I. R.: On the sensitivity of soil-vegetation-atmosphere transfer (SVAT) schemes: equifinality and the problem of robust calibration, *Agr. Forest Meteorol.*, 86, 63–75, 1997.
- Galleguillos, M., Jacob, F., Prévot, L., French, A., and Lagacherie, P.: Comparison of two temperature differencing methods to estimate daily evapotranspiration over a Mediterranean vineyard watershed from ASTER data, *Remote Sens. Environ.*, 115, 1326–1340, doi:10.1016/j.rse.2011.01.013, 2011a.
- Galleguillos, M., Jacob, F., Prévot, L., and Liang, S.: Mapping daily evapotranspiration over a Mediterranean vineyard watershed, *IEEE Geosci. Remote Sens. Lett.*, 8, 168–172, doi:10.1109/LGRS.2010.2055230, 2011b.
- Gillespie, A., Rokugawa, S., Matsunaga, T., Cothorn, S., Hook, S., and Khale, A.: A temperature and emissivity separation algorithm for Advanced Spaceborne Thermal Emission and Reflection (ASTER) images, *IEEE T. Geosci. Remote*, 36, 1113–1126, 1998.
- Gillies, R. R., Carlson, T. N., Cui, J., Kustas, W. P., and Humes, K. S.: A verification of the 'triangle' method for obtaining surface soil water content and energy fluxes from remote measurements of the Normalized Difference Vegetation Index (NDVI) and surface radiant temperature, *Int. J. Remote Sens.*, 18, 3145–3166, 1997.
- Gómez, M., Olioso, A., Sobrino, J. A., and Jacob, F.: Retrieval of evapotranspiration over the Alpillis/ReSeDA experimental site using airborne POLDER sensor and a thermal camera, *Remote Sens. Environ.*, 96, 399–408, 2005.
- Gowda, P. H., Chavez, J. L., Colaizzi, P. D., Evett, S. R., Howell, T. A., and Tolck, J. A.: ET mapping for agricultural water management: present status and challenges, *Irrig. Sci.*, 26, 223–237, doi:10.1007/s00271-007-0088-6, 2008.
- Gutman, G. and Ignatov, A.: The derivation of the green vegetation fraction from NOAA/AVHRR data for use in numerical weather prediction models, *Int. J. Remote Sens.*, 19, 1533–1543, 1998.
- Jiang, L. and Islam, S.: A methodology for estimation of surface evapotranspiration over large areas using remote sensing observations, *Geophys. Res. Lett.*, 26, 2773–2776, 1999.
- Jiang, L. and Islam, S.: An intercomparison of regional latent heat flux estimation using remote sensing data, *Int. J. Remote Sens.*, 24, 2221–2236, 2003.
- Julien, Y. and Sobrino, J. A.: The Yearly Land Cover Dynamics (YLCD) method: an analysis of global vegetation from NDVI and LST parameters, *Remote Sens. Environ.*, 113, 329–334, doi:10.1016/j.rse.2008.09.016, 2009.
- Kalma, J. D., McVicar, T. R., and McCabe, M. F.: Estimating land surface evaporation: a review of methods using remotely

- sensed surface temperature data, *Surv. Geophys.*, 29, 421–469, doi:10.1007/s10712-008-9037-z, 2008.
- Kim, J. and Hogue, T. S.: Improving spatial soil moisture representation through integration of AMSR-E and MODIS products, *IEEE T. Geosci. Remote*, 50, 446–460, doi:10.1109/TGRS.2011.2161318, 2012.
- Kustas, W. P. and Anderson, M. C.: Advances in thermal infrared remote sensing for land surface modeling, *Agr. Forest Meteorol.*, 149, 2071–2081, doi:10.1016/j.agrformet.2009.05.016, 2009.
- Kustas, W. P. and Daughtry, C. S. T.: Estimation of the soil heat flux/net radiation ratio from spectral data, *Agr. Forest Meteorol.*, 49, 205–223, 1989.
- Lagouarde, J.-P., Bach, M., Sobrino, J. A., Boulet, G., Briottet, X., Cherchali, S., Coudert, B., Dadou, I., Dedieu, G., Gamet, P., Hagolle, O., Jacob, F., Nerry, F., Olioso, A., Otlé, C., Roujean, J.-L., and Fargant, G.: The MISTIGRI thermal infrared project: scientific objectives and mission specifications, *Int. J. Remote Sens.*, 34, 3437–3466, 2013.
- Li, Z.-L., Tang, R., Wan, Z., Bi, Y., Zhou, C., Tang, B., Yan, G., and Zhang, X.: A review of current methodologies for regional evapotranspiration estimation from remotely sensed data, *Sensors*, 9, 3801–3853, doi:10.3390/s90503801, 2009.
- Long, D. and Singh, V. P.: A two-source trapezoid model for evapotranspiration (TTME) from satellite imagery, *Remote Sens. Environ.*, 121, 370–388, doi:10.1016/j.rse.2012.02.015, 2012.
- Long, D. and Singh, V. P.: Assessing the impact of end-member selection on the accuracy of satellite-based spatial variability models for actual evapotranspiration estimation, *Water Resour. Res.*, 49, 2601–2618, doi:10.1002/wrcr.20208, 2013.
- Long, D., Singh, V. P., and Scalon, B. R.: Deriving theoretical boundaries to address scale dependencies of triangle models for evapotranspiration estimation, *J. Geophys. Res.*, 117, D05113, doi:10.1029/2011JD017079, 2012.
- Mallick, K., Bhattacharya, B. K., and Patel, N. K.: Estimating volumetric surface moisture content for cropped soils using a soil wetness index based on surface temperature and NDVI, *Agr. Forest Meteorol.*, 149, 1327–1342, doi:10.1016/j.agrformet.2009.03.004, 2009.
- Margulis, S. A., Kim, J., and Hogue, T.: A comparison of the triangle retrieval and variational data assimilation methods for surface turbulent flux estimation, *J. Hydrometeorol.*, 6, 1063–1072, 2005.
- McVicar, T. R. and Jupp, D. L. B.: Estimating one-time-of-day meteorological data from standard daily data as inputs to thermal remote sensing based energy balance models, *Agr. Forest Meteorol.*, 96, 219–238, 1999.
- McVicar, T. R. and Jupp, D. L. B.: Using covariates to spatially interpolate moisture availability in the Murray-Darling basin: a novel use of remotely sensed data, *Remote Sens. Environ.*, 79, 199–212, 2002.
- Menenti, M., Bastiaanssen, W., van Eick, D., and Abd el Karim, M. A.: Linear relationships between surface reflectance and temperature and their application to map actual evaporation of groundwater, *Adv. Space Res.*, 9, 165–176, 1989.
- Merlin, O. and Chehbouni, G.: Different approaches in estimating heat flux using dual angle observations of radiative surface temperature, *Int. J. Remote Sens.*, 25, 275–289, 2004.
- Merlin, O., Walker, J. P., Chehbouni, A., and Kerr, Y.: Towards deterministic downscaling of SMOS soil moisture using MODIS derived soil evaporative efficiency, *Remote Sens. Environ.*, 112, 3935–3946, doi:10.1016/j.rse.2008.06.012, 2008.
- Merlin, O., Duchemin, B., Hagolle, O., Jacob, F., Coudert, B., Chehbouni, G., Dedieu, G., Garatuza, J., and Kerr, Y.: Disaggregation of MODIS Surface Temperature over an Agricultural Area Using a Time Series of Formosat-2 Images, *Remote Sens. Environ.*, 114, 2500–2512, doi:10.1016/j.rse.2010.05.025, 2010.
- Merlin, O., Jacob, F., Wigneron, J.-P., Walker, J., and Chehbouni, G.: Multi-dimensional disaggregation of land surface temperature using high-resolution red, near-infrared, shortwave-infrared and microwave-L bands, *IEEE T. Geosci. Remote*, 50, 1864–1880, doi:10.1109/TGRS.2011.2169802, 2012a.
- Merlin, O., Rüdiger, C., Al Bitar, A., Richaume, P., Walker, J., and Kerr, Y.: Disaggregation of SMOS soil moisture in south-eastern Australia, *IEEE T. Geosci. Remote*, 50, 1556–1571, doi:10.1109/TGRS.2011.2175000, 2012b.
- Merlin, O., Chirouze, J., Olioso, A., Jarlan, L., Chehbouni, G., and Boulet, G.: An image-based four-source surface energy balance model to estimate crop evapotranspiration from solar reflectance/thermal emission data (SEB-4S), *Agr. For. Meteorol.*, under review, 2013a.
- Merlin, O., Escorihuela, M. J., Mayoral, M. A., Hagolle, O., Al Bitar, A., and Kerr, Y.: Self-calibrated evaporation-based disaggregation of SMOS soil moisture: an evaluation study at 3 km and 100 m resolution in Catalunya, Spain, *Remote Sens. Environ.*, 130, 25–38, doi:10.1016/j.rse.2012.11.008, 2013b.
- Monteith, J. L.: *Principles of environmental physics*, Edward Arnold Press, London, 1973.
- Moran, M. S., Clarke, T. R., Inoue, Y., and Vidal, A.: Estimating crop water deficit using the relation between surface-air temperature and spectral vegetation index, *Remote Sens. Environ.*, 49, 246–263, 1994.
- Nemani, R. R. and Running, S. W.: Estimation of regional surface resistance to evapotranspiration from NDVI and thermal-IR AVHRR data, *J. Appl. Meteorol.*, 28, 276–284, 1989.
- Noilhan, J. and Planton, S.: A simple parameterization of land surface processes for meteorological models, *Mon. Weather Rev.*, 117, 536–549, 1989.
- Norman, J. M., Kustas, W. P., and Humes, K. S.: A two-source approach for estimating soil and vegetation energy fluxes in observations of directional radiometric surface temperature, *Agr. Forest Meteorol.*, 77, 263–293, 1995.
- Ogawa, K. and Schmugge, T.: Mapping surface broadband emissivity of the Sahara desert using ASTER and MODIS data, *Earth Interact.*, 8, 1–14, 2004.
- Olioso, A., Inoue, Y., Ortega-Farias, S., Demarty, J., Wigneron, J.-P., Braud, I., Jacob, F., Lecharpentier, P., Otlé, C., Calvet, J.-C., and Brisson, N.: Future directions for advanced evapotranspiration modeling: assimilation of remote sensing data into crop simulation models and SVAT models, *Irrig. Drain. Syst.*, 19, 377–412, 2005.
- Pipunic, R. C., Walker, J. P., and Western, A.: Assimilation of remotely sensed data for improved latent and sensible heat flux prediction: a comparative synthetic study, *Remote Sens. Environ.*, 112, 1295–1305, doi:10.1016/j.rse.2007.02.038, 2008.
- Price, J. C.: Using spatial context in satellite data to infer regional scale evapotranspiration, *IEEE T. Geosci. Remote*, 28, 940–948, 1990.

- Roerink, G. J., Su, Z., and Menenti, M.: S-SEBI: a simple remote sensing algorithm to estimate the surface energy balance, *Phys. Chem. Earth*, 25, 147–157, 2000.
- Sandholt, I., Rasmussen, K., and Andersen, J.: A simple interpretation of the surface temperature/vegetation index space for assessment of surface soil moisture status, *Remote Sens. Environ.*, 79, 213–224, 2002.
- Schmugge, T. J., Hook, S. J., and Coll, C.: Recovering surface temperature and emissivity from thermal infrared multispectral data, *Remote Sens. Environ.*, 65, 121–131, 1998.
- Sobrino, J. A., Gómez, M., Jiménez-Munoz, J. C., Olioso, A., and Chehbouni, G.: A simple algorithm to estimate evapotranspiration from DAIS data: application to the DAISEX campaigns, *J. Hydrol.*, 315, 117–125, doi:10.1016/j.jhydrol.2005.03.027, 2005.
- Sobrino, J. A., Gómez, M., Jiménez-Munoz, J. C., and Olioso, A.: Application of a simple algorithm to estimate daily evapotranspiration from NOAA-AVHRR images for the Iberian Peninsula, *Remote Sens. Environ.*, 110, 139–148, doi:10.1016/j.rse.2007.02.017, 2007.
- Stisen, S., Sandholt, I., Nørgaard, A., Fensholt, R., and Jensen, K. H.: Combining the triangle method with thermal inertia to estimate regional evapotranspiration – Applied to MSG-SEVERI data in the Senegal River basin, *Remote Sens. Environ.*, 112, 1242–1255, 2008.
- Su, Z.: The Surface Energy Balance System (SEBS) for estimation of turbulent heat fluxes, *Hydrol. Earth Syst. Sci.*, 6, 85–100, doi:10.5194/hess-6-85-2002, 2002.
- Tang, R., Li, Z.-L., and Tang, B.: An application of the Ts-VI method with enhanced edges determination for evapotranspiration estimation from MODIS data in arid and semi-arid regions: Implementation and validation, *Remote Sens. Environ.*, 114, 540–551, doi:10.1016/j.rse.2009.10.012, 2010.
- Tanguy, M., Baille, A., González-Real, M. M., Lloyd, C., Capelaere, B., Kergoat, L., and Cohard, J.-M.: A new parameterisation scheme of ground heat flux for land surface flux retrieval from remote sensing information, *J. Hydrol.*, 454–455, 113–122, doi:10.1016/j.jhydrol.2012.06.002, 2012.
- Timmermans, W. J., Kustas, W. P., Anderson, M. C., and French, A. N.: An intercomparison of the Surface Energy Balance Algorithm for Land (SEBAL) and the Two-Source Energy Balance (TSEB) modeling schemes, *Remote Sens. Environ.*, 108, 369–384, doi:10.1016/j.rse.2006.11.028, 2007.
- Venturini, V., Bisht, G., Islam, S., and Jiang, L.: Comparison of evaporative fractions estimated from AVHRR and MODIS sensors over South Florida, *Remote Sens. Environ.*, 93, 77–86, doi:10.1016/j.rse.2004.06.020, 2004.
- Verstraeten, W. W., Veroustraete, F., and Feyen, J.: Assessment of evapotranspiration and soil moisture content across different scales of observation, *Sensors*, 8, 70–117, 2008.
- Wan, Z., Wang, P., and Li, X.: Using MODIS land surface temperature and normalized difference vegetation index products for monitoring drought in the southern Great Plains, USA, *Int. J. Remote Sens.*, 25, 61–72, 2004.
- Weiss, M., Baret, F., Leroy, M., Begué, A., Hautecoeur, O., and Santer, R.: Hemispherical reflectance and albedo estimates from the accumulation of across track sun synchronous satellite data, *J. Geophys. Res.*, 104, 221–232, 1999.
- Yang, Y. and Shang, S.: A hybrid dual-source scheme and trapezoid framework-based evapotranspiration model (HTEM) using satellite images: algorithm and model test, *J. Geophys. Res.-Atmos.*, 118, 2284–2300, doi:10.1002/jgrd.50259, 2013.